ACS SENSORS

pubs.acs.org/acssensors

Article

Magnetoresistive Sensor in Two-Dimension on a 25 μm Thick Silicon Substrate for In Vivo Neuronal Measurements

Chloé Chopin, Jacob Torrejon, Aurélie Solignac, Claude Fermon, Patrick Jendritza, Pascal Fries, and Myriam Pannetier-Lecoeur*

Cite This: https://dx.doi.org/10.1021/acssensors.0c01578

Read Online

ACCESS | Metrics & More | Article Recommendations

ABSTRACT: Neuronal electrical activity is widely studied in vivo, and the ability to measure its magnetic equivalent to obtain an undisturbed signal with both amplitude and direction information leading to neuronal signal mapping would be a promising tool for neuroscience. To provide such a tool, a probe with spin-electronics-based magnetic sensors with orthogonal axes of sensitivity for two directions of measurement is realized, thanks to a local magnetization re-orientation technique induced by Joule heating. This probe is tested under in vivo measurement conditions in the brain of an anesthetized rat. To be as close as possible to neurons and to create minimal damage during the probe's insertion, the tip thickness has been drastically decreased using a silicon-on-insulator substrate. Our probes provide the ability to perform in vivo magnetic measurements on two orthogonal axes on a 25 μm thick silicon tip with a sensitivity of 1.7%/mT along one axis and 0.9%/mT along the perpendicular axis in the sensor plane, for a limit of detection at 1 kHz of 1.0 and 1.3 nT, respectively. These probes have been tested through a phantom study and during an in vivo experiment. The robustness and stability over one year are demonstrated.

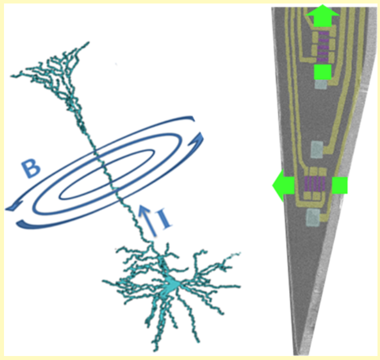

KEYWORDS: *giant magneto-resistance (GMR), biosensor, magnetoresistive sensors, bidirectional imaging, silicon-on-insulator*

Neuronal activity is widely studied both at the macro-scale with electroencephalography or magnetoencephalography (MEG) and at the micro-scale with single electrodes or arrays of electrodes. Until recently, micro-scale recordings in vivo were limited to electric signals.[1,2] Accessing local magnetic fields brings several advantages. Unlike electric signals, which have to be referenced, magnetic measurements are reference-free. Furthermore, magnetic signals are not disturbed by the change of conductivity in the different parts of the brain,[3] and they may provide information about both amplitude and direction of the neuronal currents, potentially leading to novel scientific insights.

At the macro-scale, for MEG studies, superconducting quantum interference devices are the sensors of choice because of their extremely low limit of detection (LOD) (around few fT/$\sqrt{\text{Hz}}$ at 1 Hz), but they require to be cooled in liquid helium[4] and thus are not appropriate for local in vivo recordings. Magnetic sensing of action potentials has already been reported for nitrogen-vacancy centers on marine worms with an LOD of 15 pT/$\sqrt{\text{Hz}}$ at 250 Hz.[5] Yet, this technique presents challenges for adaptation to local in vivo recordings in mammalian brains because of the size and embodiment of the optical excitation and detection setup.

A first proof-of-concept for local recording of magnetic activity of muscle has been realized with giant magneto-resistance (GMR) sensors[6] with spin-valve configuration.[7] Such sensors are biocompatible, offer a good sensitivity at physiological temperature (around 1.5−2%/mT), and can be miniaturized down to micron scale. In previous work, local in vivo recordings of magnetic signals associated with visually evoked potentials have been achieved with the help of "magnetrodes", sharp probes, containing GMR sensors that could be inserted into in vivo[8] or in vitro[9] brain tissues.

For a detailed biophysical and circuit-level understanding, the ultimate goal would be to achieve single neuron activity recordings and benefit from the directional information given by magnetic recordings. This would not only help us to localize multiple neurons that would be otherwise inseparable in electrical recordings but also potentially allow for a better understanding of the underlying electrical currents in local brain circuits. For this purpose, we developed sharp probes with several magnetic sensors suitable for recording of neuronal magnetic signals with two axes of sensitivity for recording two spatial components of the magnetic field. Our goal was to record spike signals generated by neurons, whose

Received: July 30, 2020
Accepted: October 16, 2020

amplitude is expected in the range of 10−100 pT at a frequency of around 1 kHz (estimated from ref 10).

The probe was designed with a tip angle of 18° and was produced from a silicon-on-insulator (SOI) wafer. This resulted in a very thin and sharp probe that should create minimal damage to the brain tissue during the insertion of the probe. It also allowed the magnetic source (neurons and synapses) to be as close as possible to the magnetic sensors. This is crucial as the magnetic field decreases quickly with distance. The probes were etched with deep reactive ion etching (RIE). Cardoso et al. developed thin probes with GMR sensors on a 50 μm thick SOI substrate, but these probes exhibited increased noise, leading to an LOD of 500 nT/$\sqrt{\text{Hz}}$ at 30 Hz,[11] which is one hundred times higher than state-of-the-art GMR sensors on conventional silicon wafers.[8,11]

We combined this improved design of the probe with features allowing 2D mapping of magnetic fields. This is achieved by setting the magnetic orientation of two GMR sensors at 90° from each other and by following a specific two-step annealing procedure during probe fabrication.

In summary, we developed a very thin (25 μm) and sharp magnetic probe for minimally traumatic insertion into the brain, with two GMR sensors having orthogonal axes of sensitivity and exhibiting an LOD in the range of few nT/$\sqrt{\text{Hz}}$ at 1 kHz, being a state-of-the-art promising tool for mapping neuronal activity.

■ MATERIALS AND METHODS

GMR Stack Composition. GMR is one experimental expression of the spin electronics principle, which relies on modification of transport properties in thin ferromagnetic layers according to their magnetic configuration. GMR sensors are generally realized following a spin valve configuration,[12,13] which assembles a reference layer with a fixed magnetization and a free layer which rotates freely with the external magnetic field. These two layers are separated by a conductive and non-magnetic layer (here copper). The reference layer is composed of a synthetic antiferromagnetic (SAF) structure (two CoFe layers coupled by Ruderman−Kittel−Kasuya−Yosida coupling through Ru[14]) which is magnetically coupled through exchange bias to an IrMn antiferromagnetic layer.[15] The free layer is composed of two soft ferromagnetic layers; here, NiFe and CoFe.

The whole GMR stack has the following composition: Ta (3 nm)/NiFe (5 nm)/CoFe (2.1 nm)/Cu (2.9 nm)/CoFe (2.1 nm)/Ru (0.85 nm)/CoFe (2 nm)/IrMn (7.5 nm)/Ru (0.4 nm)/Ta (5 nm).

The GMR stack is deposited by sputtering (Rotaris deposition chamber from Singulus) on an SOI substrate which is composed of SiO_2 (500 nm)/Si (25 μm)/SiO_2 (2 μm)/Si (400 μm)/SiO_2 (2 μm).

After the GMR stack deposition, an oven annealing at 1 T and 180 °C is performed to set the magnetization direction of the reference layer perpendicularly to the magnetrode tip direction (Figure 1a). The annealing field and temperature optimization are a compromise. The temperature has to be above the IrMn exchange bias blocking temperature (180 °C) but below the atomic diffusion.[15] The field has to be high enough to orient completely the CoFe magnetization in contact with IrMn and to break the SAF coupling.

In order to have a linear response around the zero applied field, the hard layer and the free layer magnetization must be perpendicular.[13] The free layer magnetization direction is set by shape anisotropy[13] along the sensor's length. For 2D recording, two sensors, M_1 and M_2, are on the magnetrode. To have perpendicular axis of sensitivity, one of the sensors is turned by an angle of 90° (Figure 1). After oven annealing only one sensor has its reference magnetization perpendicular to the one of the free layer (M_1 on Figure 1a). M_2 needs a local repinning to force the reference layer magnetization at 90° which is done at the very end of the process.

Magnetrode Fabrication and Method for Decreasing Tip Thickness. GMR sensors are shaped by optical lithography and Ar ion milling into two meanders oriented at 90° with regard to each other and separated, center-to-center, by 255 μm (Figure 1). In order to increase the magnetic volume and thus to reduce the $1/f$ noise, sensors are meander shaped.[16] They are composed of 5 stripes with a length of 54 μm and a width of 4 μm. The bars are connected in series by Ti (5 nm)/Au (130 nm)/Ti (5 nm) contacts evaporated on top of the GMR leading to an effective sensor magnetic length of 30 μm. The sensors are then protected by a sputtered passivating bilayer of Al_2O_3 (150 nm)/Si_3N_4 (150 nm). A combination of front/back side and RIE/deep RIE are used to define the magnetrode tip (227 μm width, 25 μm thick). The deep RIE uses a Bosch process[17] to perform highly-anisotropic etches of thick silicon films by alternating two steps: a chemical SF_6-based etching and a deposition of a chemically inert C_4F_8 passivation layer. The oxide films are removed by RIE based on O_2 and SF_4 plasma. The first magnetrode tip process step consists in defining the shape of the probe from the front side; the passivation bilayer and the top SiO_2 of the SOI are etched by RIE, and the 25 μm SOI silicon is etched by deep RIE. Then, the tip probes are thinned and separated from the back side. The 2 μm SOI oxide in the backside is removed by RIE, the 400 μm thick silicon layer (400 μm) is etched by deep RIE, and finally, the SiO_2 buried layer is etched by RIE for probe release. During deep RIE, to ensure a good thermal contact between the wafer and the baking wafer, a Fomblin thermal grease is used. 3M Novec 7200 was used to clean the holding grease after deep RIE. The magnetrodes are then mounted on a printed circuit board (PCB) and wire bonded.

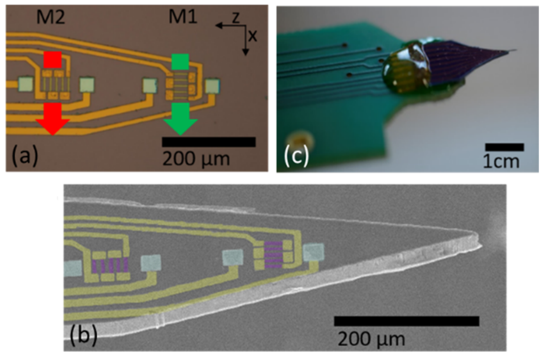

Figure 1. Magnetrode with a thinned tip and two orthogonal GMR sensors (M_1 and M_2). (a) Optical microscope image of sensors after electrode deposition. Arrows represent magnetic orientation of the reference layer after initial oven annealing of the wafer. Green arrow indicates that the layer is well oriented (M_1 sensor); red arrow indicates that the sensor needs a local repinning to have perpendicular magnetic orientation between the reference and free layer at zero-field (M_2 sensor). (b) Scanning electronic microscopy image of the magnetrode's tip in false colors. Contacts appear in yellow and GMR meander strips appear in purple. Platinum electrodes (white color) have also been deposited, though not used during the in vivo experiment, but replaced by dense arrays of electrodes. (c) Optical picture of the 2D magnetrode mounted on a PCB. Aluminum wire bondings are encapsulated in Araldite paste. Only the tip of the probe, over a length of 2.0 mm, is thinned down to 25 μm, while the rest of the tip remaining around 400 μm thick.

Magnetotransport and Noise Characterization of the Probes. Magnetotransport measurements are performed with a two-point measurement setup, as described in Figure 2. GMR sensors are powered by a 1 mA current using a Keithley ultra-sensitive current source (Series 6221); the output voltage is amplified and filtered at 30 Hz by a low-noise amplifier (SR560—Stanford Research Systems) and sent to the acquisition card (DT 9836—Data Translation). An external field is applied parallel to the sensor axis of sensitivity between ±20 mT by Helmholtz coils. The magneto resistance (MR) ratio and sensitivity are extracted from the resistance versus field sensor transfer curves,[18,19] one typical example is shown in Figure 2b. If R_P is the resistance in the parallel state (free and reference layer

https://dx.doi.org/10.1021/acssensors.0c01578
ACS Sens. XXXX, XXX, XXX−XXX

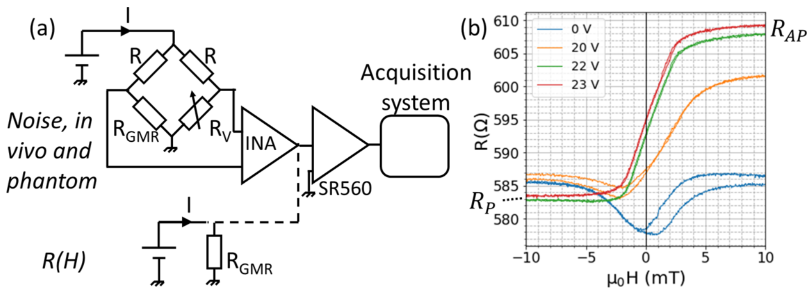

Figure 2. (a) Schematic illustration of the setups for magnetotransport ($R(H)$), in vivo/phantom and noise measurement. (b) Resistance vs field curve as function of the applied voltage during the local repinning of sensor M_2. The field is applied (880 mT) along the z direction (90°).

magnetization are parallel) and R_{AP} is the resistance in the antiparallel state, the MR ratio (%) and the sensitivity S (%/mT) are defined by

$$\mathrm{MR} = \frac{R_{AP} - R_P}{R_0} \times 100; \qquad S = \frac{\delta R}{\delta H} \cdot \frac{1}{R_0} \times 100;$$

$$R_0 = \frac{R_{AP} + R_P}{2}$$

Noise measurements are achieved in a magnetically shielded room; each sensor is characterized in a Wheatstone bridge that includes the GMR element and a variable resistance (Figure 2). Both outputs are sent in differential mode to a low noise amplifier (INA 103—Texas Instrument). The output signal is then amplified and filtered (0.3 Hz to 3 kHz) by a low-noise amplifier (SR 560—Stanford Research Systems) on a battery to avoid 50 Hz power line contamination. The bridge is powered by a battery so that GMR bias voltage is 1 V. A calibration coil powered by an AC current typically at 30 Hz is used to apply a calibrated field and to extract the sensor sensitivity from the noise spectrum density.[18,19] The LOD is then defined as noise divided by sensitivity.

Local Repinning. The last step for the 2D magnetrode fabrication consists of local repinning of the reference layer from sensor M_2 on the probe (red arrow in Figure 1). As explained previously, free layer magnetization direction at zero field is determined by the sensor shape (along x for M_1 and along z for M_2), and the reference layer has to be perpendicular to the free layer at zero field. After oven annealing, the M_1 reference layer is magnetized in the proper direction (along x and perpendicular to the free layer arm length), while the M_2 reference layer needs to be reoriented along the z direction.

Local repinning consists in annealing M_2 by Joule heating with a voltage pulse under a strong magnetic field applied along z. The voltage pulse is generated using a high voltage pulse generator (GI SAU-P102—Systems Development & Solutions). To set the optimized repinning parameters (voltage amplitude and duration), resistance and sensitivity are evaluated after each pulse by magnetotransport measurements, as presented in Figure 2b. The optimal intensity of the voltage pulse is a compromise between exchange bias repinning of the reference layer and sensor thermal degradation. Experimentally, the optimal repinning conditions (23 V, 80 μs, under 880 mT) correspond to the maximal MR measured in the transfer curve before degradation, seen by the increase of the resistance in the parallel state R_P (Figure 2b).

Phantom. In order to test the probes when exposed to a local magnetic field, we fabricated a phantom comprising of thin aluminum wires (diameter 25 μm), two wires being oriented perpendicular to each other along x and z direction and a single wire positioned roughly with an angle of 45° regarding the x axis. The probe is located on a plane parallel to the wire(s) at a relatively close distance (on the order of 2 mm), as depicted in Figure 3. The wires are fed with a sinusoidal current which can vary in amplitude (10 μA to 10 mA) and in frequency (0.8−1 kHz). As each wire is powered individually and is isolated from the other, test fields with an arbitrary angle and amplitude can also be generated. The output voltage of each sensor is recorded by using two separated acquisition setups described in Figure 2a. The temporal signal and the power spectral density are acquired for each sensor, and the signal amplitude is extracted from the signal peak in the frequency domain. An average of over 10 measurements is also performed to avoid random and undesirable glitches in the output.

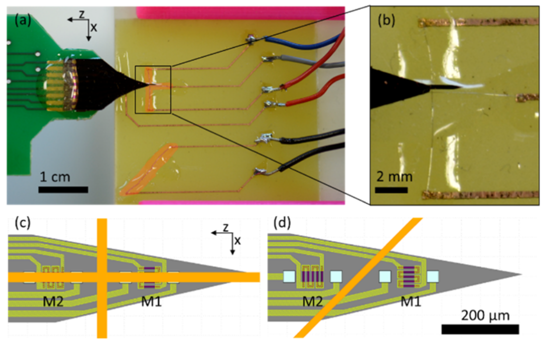

Figure 3. Phantom setup used to test the 2D-recording of the magnetrode. (a) View of the experimental setup with the magnetrode located in near vicinity to the thin wires highlighted in orange. The wires are positioned along x direction, z direction, and at 45°. (b) Zoom on probe tip and wires. (c,d) Schematic of the wire positions relative to sensors M_1 and M_2.

In Vivo Measurements. Two adult male Sprague Dawley rats (*Rattus norvegicus* domestica) were used in this study. All experimental procedures were in accordance with the animal welfare guidelines of the Regional Board Darmstadt (F149/2004) and the "European Union's Directive 2010/63/EU". Animals were anesthetized initially with a mixture of ketamine (80 mg/kg) and medetomidine (0.01 mg/kg) and then maintained with isoflurane (1−2% in 100% oxygen) via a custom face mask. Analgesia was maintained with regular injections of buprenorphine (0.03 mg/kg). Animals were also injected with dexamethasone (1 mg/kg) to prevent brain swelling and with a mixture of amino acids and glucose to maintain their physiological state.

In order to validate functionality under in-vivo experimental conditions, thin (25 μm) and thick (270 μm) probes were tested in the brain of anesthetized rats by using the setup described in Figure 4. In order to minimize external noise contamination, the animal and a part of the readout electronics were installed inside an aluminum shielding box which acts as a Faraday cage. All electronics inside the box were powered by batteries to avoid 50 Hz power-line noise. All data connections between electronics inside and outside the box were made through optical wires. Vitals of the rat were monitored through electrocardiogram, respiration, and temperature.

To record electrical neural activity from neurons in the close vicinity of the GMR sensors, a commercial NeuroNexus electrode array (Cat#$A_{1\times32}$-$Poly_2$-5mm-50s-177) [https://neuronexus.com] or FHC tungsten microelectrodes (Cat#$UEWMEGSECN_3M$) [https://www.fh-co.com/product/metal-microelectrodes/] were attached on the probe tip. In the case of the electrode array (Figure 4b), the electrode contacts were placed directly above the lower sensor. The

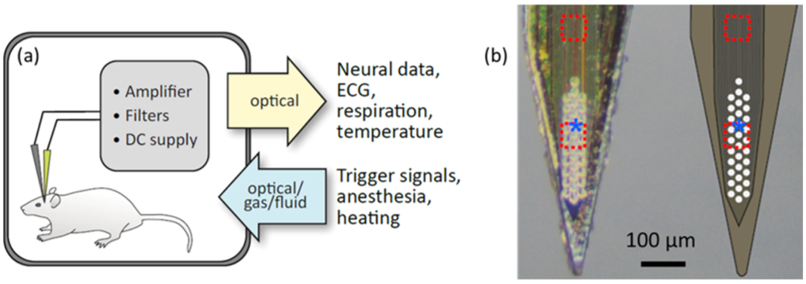

Figure 4. In vivo recording setup. (a) Schematic of the experiment. The animal and a part of the electronics for the magnetrode are placed in a Faraday cage. Data are then transmitted through optical wires. Monitoring of the animal is placed outside of the shielding box. (b) Electrode placement and design relative to the probe. Position of GMR sensors indicated by red dashed boxes. Blue points indicate electrode location for recordings shown in Figure 7.

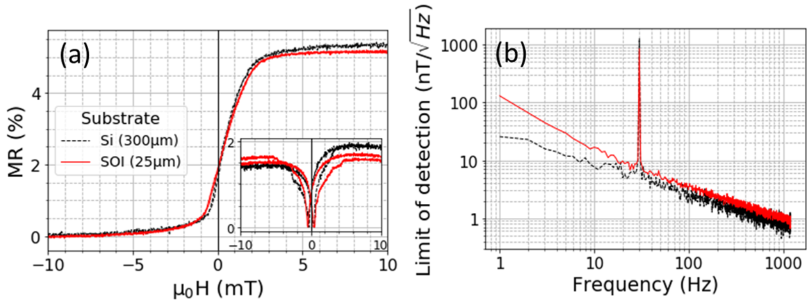

Figure 5. Comparison of sensor's characteristics depending on the substrate: 270 μm thick Si magnetrodes (black dash line) and 25 μm thick SOI magnetrodes (red line). (a) Sensor's response to an external field along its sensitivity axis. Inset: Sensor's response to an external field perpendicular to its sensitivity axis for both substrates (b) LOD of a GMR sensor along its sensitivity axis (0.95 nT at 1 kHz for Si substrate and 1 nT for SOI substrate). At 30 Hz, a calibration peak is used to compute sensor's sensitivity.

Table 1. Comparison of MR, Sensitivity, the LOD at 1 kHz along Their Main Sensitivity Axis for M_1 and M_2 Sensors on the SOI Substrate, and Respective Standard Deviation Averaged over 5 Probes Containing Two Orthogonal Sensors

sensor	M_1 main sensitivity axis x – 0°		M_2 main sensitivity axis z – 90°	
MR (%)	5.4 ± 0.1		4.6 ± 0.3	
direction of measurement	x (0°)	z (90°)	x (0°)	z (90°)
sensitivity (%/mT)	S_{1x} = 1.77 ± 0.13	S_{1z} = 0.94 ± 0.07	S_{2x} = 0.25 ± 0.04	S_{2z} = 0.97 ± 0.08
LOD (nT/$\sqrt{\text{Hz}}$)	1.5 ± 0.3		2.9 ± 0.9	

GMR signal was measured through the same electronics scheme as for noise measurements, with an amplification of typical gain 1000 and filtered in the 10 Hz to 3 kHz band (Figure 2). Signals from the GMR sensors and the electrodes were buffered by a unity gain head-stage and digitized at 24,414.0625 Hz with a standard acquisition system (Tucker Davis Technologies, USA).

During recordings, the 1−2 V bias voltage to the GMR sensors were controlled via an external TTL signal. This allows having a control sequence to check for direct capacitive coupling to the GMR of the electrical signal in the tissues. The TTL signal was converted into an optical signal via a custom circuit to reduce external noise. Inside the shielding box, the optical signal was converted back to an electrical signal to control the voltage bias to the GMR sensors from a battery.

Analysis of Firing Rate Differences. Two recording blocks per condition from the same animal were analyzed for spiking activity. Each recording was bandpass filtered with a 2nd order Butterworth filter (0.3−6 kHz). Thresholds (Thr) for spike detection were calculated according to ref 20 as

$$\mathrm{Thr} = 5\sigma_n; \qquad \sigma_n = \mathrm{median}\left\{\frac{|x|}{0.6745}\right\}$$

where x is the filtered signal and σ_n is the estimate of the standard deviation of the background noise.

Each recording block was split into non-overlapping epochs of 1 s duration, and firing rates were calculated for every epoch. This resulted in n = 2587 and n = 1988 epochs for the "thick" and "thin" condition, respectively. Confidence intervals were calculated by bootstrapping across epochs (10,000 bootstrap replications).

RESULTS AND DISCUSSION

Magnetrodes Performances. Several magnetrodes carrying two sensors with orthogonal reference were fabricated and characterized with regard to magnetotransport and noise to evaluate their performances. Figure 5 shows the RH curve at room temperature and the noise spectral density, both being compared with the same GMR stack sensor deposited on a thick (270 μm) conventional silicon substrate and submitted to the same post-deposition annealing procedure. Table 1 details MR, sensitivity, and LOD along the two in-plane axes (0 and 90°). The RH ratios are extracted from the resistance versus field curve. The sensitivity and LOD are extracted from the noise data.

We observed at first that magnetrodes with a tip thickness of 25 μm had a sensitivity ranging from 1.5 to 2%/mT and an LOD around 1.5 nT/$\sqrt{(\text{Hz})}$ at 1 kHz, which is close to typical values measured on thick silicon probes (respectively 1.9 ± 0.1%/mT and 1.4 ± 0.3 nT/$\sqrt{(\text{Hz})}$ averaged over 6 probes and 13 sensors).

https://dx.doi.org/10.1021/acssensors.0c01578
ACS Sens. XXXX, XXX, XXX−XXX

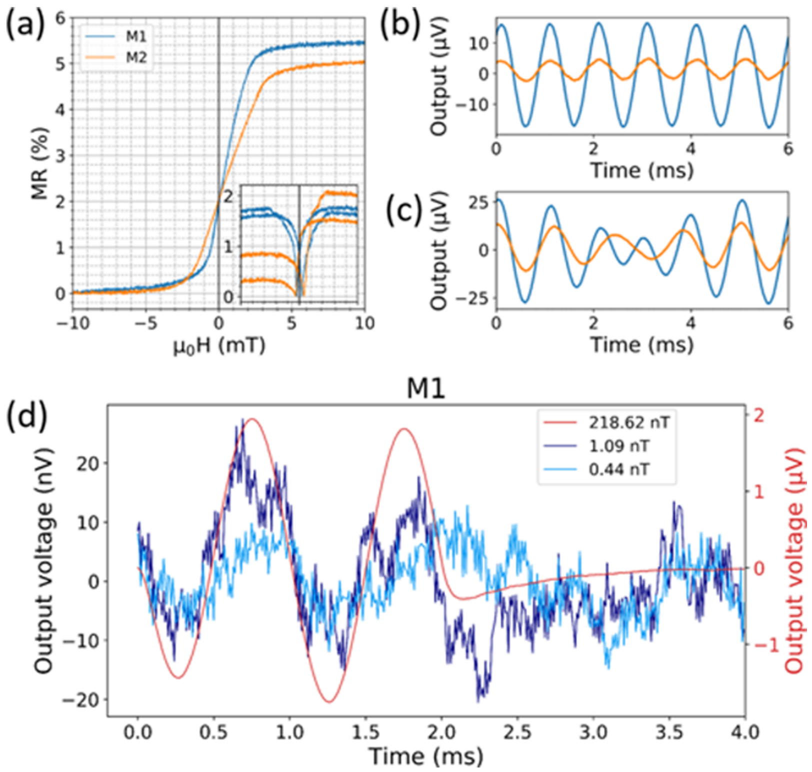

Figure 6. (a) Comparison of sensor's characteristics after M_2 local repining along their sensitivity axis and at 90° (inset). M_1 pinning is achieved by a global repining, while M_2 is locally repinned. MR in M_2 is slightly lower than M_1 (5.1% vs 5.5%). The slope around the zero field of M_2 is lower than M_1, leading to a reduced sensitivity as well (0.92 %/mT vs 1.70%/mT). (b,c) Output voltage in μV on M_1 and M_2 with a magnetic field generated by a wire at 0° powered by a current of 9.8 mA at 1 kHz (b) and when the wire at 0° is powered by 9.8 mA at 1 kHz and the wire at 90° is powered by 12.1 mA at 800 Hz (c). The signal on the sensors is thus a combination of the two fields. For both graphs, the signal is averaged over 10 measurements. (d) Output voltage on M_1 for a sinusoidal current (2 periods) feeding the 0° wire with amplitudes corresponding to a field of 218 nT, 1.09 nT, and 440 pT. Signal here is averaged 40,000 times.

No random telegraphic noise (RTN) is observed up to 2 V biasing, which can allow the use of a large bias voltage to increase the output signal (which is of interest when detecting signal in the thermal noise regime, i.e., here, above 1 kHz, which is the frequency range containing most energy of neuronal action potentials). Thus, the manufacturing process of the fine tips has made it possible to obtain state-of-the-art probes.

Considering the impact of the repinning procedure on the sensor's performances, the maximal MR reached by M_2 with a local repining is in average slightly lower than the one achieved for M_1 with a global annealing (4.6 ± 0.3% vs 5.4 ± 0.1%) as illustrated for one probe in Figure 6a. The sensitivity is also reduced: 0.97 ± 0.08%/mT versus 1.77 ± 0.13%/mT. In the literature, MR lowered by about 25% has been reported on laser-repinned TMR sensors[21] without presenting sensitivity or noise comparison on their repinned structures. These differences could be explained by an incomplete repinning of the hard layer or a degradation of the GMR properties due to Joule heating. As described in Figure 2b, the local repinning is stopped at 23 V, that is, the optimal heating to achieve the highest MR and sensitivity values, while preventing any degradation of MR (characterized by an increase of resistance in the parallel state). A small hysteresis appears in the sensor's response at 90° from the sensitivity axis (Figure 6b) and could create an impact on the field reconstruction if a field higher than 5 mT is applied to the magnetrode. These fields are typically not reached in standard laboratory conditions.

The 2D magnetrode response curve can be described through the sensitivity matrix defined from Table 1 as

$$S = \begin{bmatrix} S_{1x} & S_{1z} \\ S_{2x} & S_{2z} \end{bmatrix} \quad (1)$$

where S_{ij} is the sensitivity of sensor i along j direction.

When a field H is applied, the voltages measured on sensors M_1 and M_2 of the 2D magnetrodes, V_{M_1} and V_{M_2}, are used to determine the field projection according to x (H_x) and z (H_z)

$$\begin{bmatrix} H_x \\ H_z \end{bmatrix} = S^{-1}\cdot\begin{bmatrix} V_{M_1} \\ V_{M_2} \end{bmatrix} = \frac{1}{\det S}\begin{bmatrix} S_{2z} & -S_{1z} \\ -S_{2x} & S_{1x} \end{bmatrix}\cdot\begin{bmatrix} V_{M_1} \\ V_{M_2} \end{bmatrix}$$
$$\text{with } \det S = S_{1x}S_{2z} - S_{2x}S_{1z} \quad (2)$$

Thus, when a magnetic field is detected by the 2D magnetrode, the measurement of signal amplitudes on sensors M_1 and M_2 (e.g., as shown in Figure 6a) allows H_x and H_z to be extracted according to eq 2. The amplitude of the magnetic field H and its angle θ with respect to the x-axis are derived from H_x and H_z using eq 3

$$H = \sqrt{H_x^{\,2} + H_z^{\,2}} \text{ and } \theta = \arctan\left(\frac{H_z}{H_x}\right) \quad (3)$$

The phantom is used to test the reconstruction of a signal measured on a 2D magnetrode, whose sensitivity matrix is $S = \begin{bmatrix} 1.7 & 1.1 \\ 0.2 & 0.9 \end{bmatrix}$, values being in %/mT.

The first phantom configuration studied consisted in a signal generated by a single wire at 0°, powered by 9.8 mA at 1 kHz (Figure 3c). The output signals were acquired on sensors M_1 and M_2 using the acquisition setup described in Figure 2a, and the signals are depicted in Figure 6a. Table 2 shows the voltages measured on M_1 and M_2 sensors, the evaluated field components, and angle and height in the 0° wire-case, as a function of the bias current in the wire and based on the eqs 2 and 3.

Table 2. Table Summarizing the (Amplitude) Output Voltage Measured on Sensor M_1 and M_2, the Field Reconstructed (H_x/H_z and H_{exp}/θ_{exp}) Generated by Different current Values Applied in the Wire at 0°[a]

I_x (mA)	19.6	9.8	1.964	0.196
V_{M_1} (nV)	33049	16183	3283	322
V_{M_2} (nV)	6441	3206	616	177
H_x (nT)	1796	875	180	8
H_z (nT)	232	120	20	17
H_{exp} (nT)	1810	883	181	19
θ_{exp} (deg)	7.35	7.83	6.34	65.15
$\boldsymbol{R_x}$ (mm)	2.17	2.22	2.16	2.08

[a]The distance ($\boldsymbol{R_x}$) between the wire and the sensor is estimated from the Biot and Savart law. Values for I, V, and $\underline{H}$ are peak-to-peak.

The phantom configuration composed by a single wire at 45° (Figure 3d) confirms the reconstruction protocol. Another interesting feature of the 2D magnetrode is the possible determination of the signal sources by their frequency. Indeed when the two phantom wires are powered by current at two different frequencies, it is possible to extract the amplitude and the direction of the two generated fields on the 2D magnetrode (Figure 6c).

Furthermore, the analysis of the sensors' outputs allows us on the one hand to determine the LOD over the frequency range of the acquisition and on the other hand to evaluate the height of the probe's tip with respect to the wires.

From Table 2, one observes that below 1 mA, the error becomes large; this is due mainly to the LOD of the probe. Since the signal is acquired on the [0.3 Hz to 3 kHz] bandwidth, integrating the $1/f$ variation of the noise spectrum density leads to a root mean square (rms) noise of 104 nT for M_1 and 115 nT for M_2 (in their main sensitivity axis), which is consistent with the results reported in Table 2.

A possible error could be added during the field reconstruction by the uncertainty in the determinant of the sensitivity matrix which depends on the presence of the non-diagonal terms of the S matrix. When these non-diagonal terms are non-null, then the determinant approaches zero, and the inversion of the matrix becomes more difficult. The non-diagonal terms correspond to the sensor sensitivity at 90° from the main sensitivity axis. Indeed, MR sensors are by design-sensitive in one direction in plane, along the direction of the reference layer pinning. Nevertheless, the sensitivity at 90° from this axis is not negligible, and it is almost 2/3 of the main sensitivity in the case of sensor M_1 and approximately 1/3 in the case of sensor M_2. The sensitivity at 90° is due to the in-plane rotation of the free layer around zero field, from one side to the other side of its easy anisotropy axis (determined by shape anisotropy along the arm length).

For an in vivo recording, the bandwidth can be fitted to the signal of interest, typically on a [300 Hz to 5 kHz] bandwidth. The corresponding LOD on a single acquisition would be of 57 nT rms, which averaged on 50,000 events would lower it down to 255 pT.

Experimentally with the phantom, we were able to detect a sinusoidal signal of 440 pT after 40,000 averaging's and by considering the [0.3 Hz to 3 kHz] bandwidth (see Figure 6d).

In the phantom experiment, the distance between the probe tip and the wire(s) is much larger than the distance that separated M_1 and M_2 sensors (2 mm vs 250 μm), so the field generated by the wires can be seen as rather homogeneous on both sensors.

Under realistic assumptions for in vivo recordings, the probe is expected to be much closer to the spiking neurons that could be detected (electrophysiological recordings explore spikes of neurons in the ~140 μm diameter volume around the electrode[22]). Therefore, the relative positioning of the two sensors at a 250 μm distance apart can be an additional issue to solve the reconstruction of the field in the plane. This distance can be reduced to 50 μm center-to-center on the same sensor size (reducing the sensor size would increase the low frequency noise floor). Another path could be to deposit two GMR stacks separated by a thick (few um) insulator, one of the stacks containing a pinned layer with IrMn and the other stack with PtMn as antiferromagnet with higher blocking temperature, so that the IrMn-GMR stack could be repinned with local heating conditions that would not affect the pinning of the PtMn-GMR sensor.

In Vivo Evaluation of the Probe. The fully characterized probes were subsequently used for in-vivo measurements in the brain of anesthetized rats. The tip of the probe was slowly inserted into the rat's brain and lowered until the electrodes

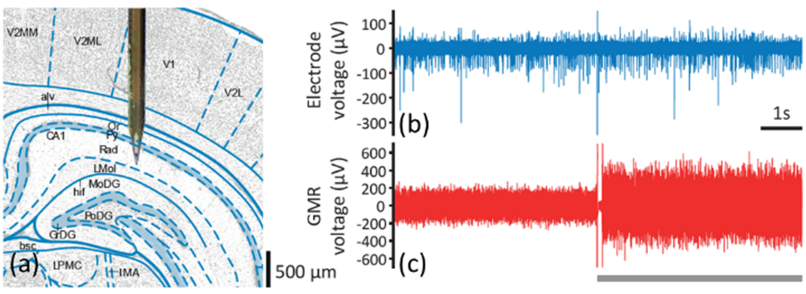

Figure 7. (a) Schematic representation of the probe inserted into the hippocampus. (b) Voltage trace of electrode showing clear neural activity. Switching artifacts are truncated at −350 and 150 μV. (c) Voltage trace of GMR sensor M_1. Gray bar indicates time of DC input to the sensor. Switching artifacts are truncated at ±−650 μV. Data in (b,c) are bandpass filtered between 0.3 and 5 kHz. Present noise is too large for a direct detection of single events.

https://dx.doi.org/10.1021/acssensors.0c01578
ACS Sens. XXXX, XXX, XXX−XXX

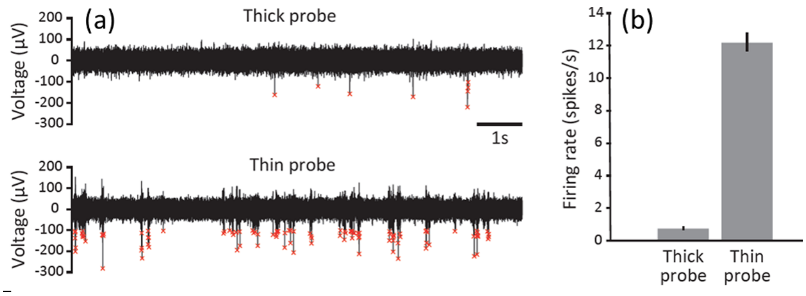

Figure 8. (a) Example of voltage traces from tungsten electrodes attached to the thick probe (upper panel) and thin probe (lower panel). Signals are bandpass filtered for spiking activity between 0.3 and 5 kHz. Red markers show detected spikes. (b) Average firing rate from the tungsten electrodes attached to the thick and thin probes. Error bars show 99th percentile bootstrap confidence intervals.

surrounding the sensor were in the pyramidal cell layer of the dorsal hippocampus (Figure 7a). Placement was confirmed by observing large amplitude extracellular spikes (Figure 7b). The hippocampus is a system of particular interest for magnetophysiology because it contains highly organized pyramidal cells, with somata and dendrites aligned in clear layers, which should provide a summation of the magnetic field. Additionally, neurons in the hippocampus exhibit a high rate of spontaneous neural activity (high firing rate of observed extracellular spikes) which could be favorable for acquiring a large number of discrete electrical events and their magnetic counterpart. In contrast to the spikes in Figure 7b, no clear magnetic spikes are visible in the voltage trace of the GMR sensor, as shown in Figure 7c. This is expected due to noise levels and sensitivity of the GMR sensor. The LOD is around 7 nT at 30 Hz and 1 nT at 1 kHz for a global rms noise in the working bandwidth [800 to 1200 Hz] of 20.6 nT without averaging. In order to have a signal-to-noise ratio of 1 for a signal of 100 pT (the expected magnetic signal generated by a neuronal action potential), the signal needs to be averaged 42,500 times. Therefore, specific spike sorting analysis to separate individual neurons from the recordings will be necessary in future work. This would allow to perform averaging over all extracellular spikes from individual neurons and might potentially reveal the magnetic signature of the electrical signal.

In Vivo Comparison of Thin and Thick Probe Design. One motivation to achieve further miniaturization of the probe was the fact that larger probe sizes can have a detrimental effect on neural tissues and therefore on the quality of neural recordings. This is true for short term effects due to more tissue displacement and for long-term effects due to immune responses.[23] In one rat, we recorded from two probe designs, the "thick" probe with a thickness of 270 μm and the "thin" probe with a thickness of 25 μm. Both probes had tungsten microelectrodes attached, which were placed such that the tip of the electrode was very close to the GMR sensor. We analyzed two recording blocks made in the hippocampus of one animal. Figure 8a shows 10 s from one of the recordings for each condition. We extracted individual spikes by setting a voltage threshold to the filtered data.[20] The average firing rate was calculated for each 1 s epoch of the recording. As can be seen from Figure 8b, the mean rate appears to be much reduced in the data recorded with the thick probe, as expected due to the large difference in probe dimensions. However, it should be noted that a detailed quantitative analysis of the impact of probe size would require a large number of recordings in multiple animals.

To evaluate the robustness of the thin probe toward insertion in tissues, which exposes it both to bending and possible corrosion by the saline medium, we compared the MR ratio and sensitivity on a probe after processing and following the in vivo experiment on 7 sensors and 3 probes. MR is very stable on average (5.39 ± 0.05 before and 5.41 ± 0.06 after) and the sensitivity is also stable (1.33 ± 0.07%/mT). In addition, between the two measurements, the magnetrodes were not exposed to a field greater than a few mT. The unchanged magnetrode properties highlight the stability over one year lifetime of the magnetrode despite a tip with a thickness of 25 μm.

■ CONCLUSIONS

In this work, a complete fabrication process of magnetrodes for in vivo applications is presented and leads to state-of-the art GMR sensor performances integrated on a 25 μm thick probe adapted for brain insertion. An additional functionality has been developed. This functionality allows 2D mapping, that is, the determination of the direction and the amplitude of the magnetic field detected by the probe and is thus highly interesting for neuroscience. The in vivo experiments performed on rat's hippocampus highlight the resistance and the long lasting of the probe in biologic liquids but also its reduced damage to the brain. Currently, the only actual limitation for magnetrode use in neuroscience is its LOD, which leads to the necessity of averaging for neuronal spike detection. However, by considering reasonable averaging, that is, over a recording session of less than 1 h (corresponding to typically around 40,000 electrical spikes recorded on an electrode inserted in the hippocampus, see Figure 8b), the LOD drops to 100 pT, which opens very interesting perspectives for this technique.

■ AUTHOR INFORMATION

Corresponding Author

Myriam Pannetier-Lecoeur − *SPEC, CEA, CNRS, Université Paris-Saclay, 91191 Gif-sur-Yvette Cedex, France;* Email: myriam.pannetier-lecoeur@cea.fr

Authors

Chloé Chopin − *SPEC, CEA, CNRS, Université Paris-Saclay, 91191 Gif-sur-Yvette Cedex, France*

Jacob Torrejon − *SPEC, CEA, CNRS, Université Paris-Saclay, 91191 Gif-sur-Yvette Cedex, France*

Aurélie Solignac − *SPEC, CEA, CNRS, Université Paris-Saclay, 91191 Gif-sur-Yvette Cedex, France;* orcid.org/0000-0002-7714-0939

Claude Fermon − *SPEC, CEA, CNRS, Université Paris-Saclay, 91191 Gif-sur-Yvette Cedex, France*

Patrick Jendritza − *Ernst Strüngmann Institute (ESI) for Neuroscience in Cooperation with Max Planck Society, 60528 Frankfurt, Germany*

Pascal Fries − *Ernst Strüngmann Institute (ESI) for Neuroscience in Cooperation with Max Planck Society, 60528 Frankfurt, Germany; Donders Institute for Brain, Cognition and Behaviour, Radboud University Nijmegen, 6525 EN Nijmegen, Netherlands*

Complete contact information is available at: https://pubs.acs.org/10.1021/acssensors.0c01578

Author Contributions

M.P.-L., P.J., and P.F. designed the research plan. C.C., J.T., M.P.-L., and A.S. designed and fabricated the sensors. C.C. performed the probe characterization and data analysis, with the help of A.S. and J.T. P.J. carried out the in vivo experiments with C.C., A.S., M.P.-L., and C.F. assisting with the data recording. C.C., A.S., and M.P.-L. wrote the manuscript with contributions from C.F., P.J., J.T., and P.F. All authors read and approved the final manuscript.

Notes

The authors declare no competing financial interest.

■ ACKNOWLEDGMENTS

This work has been funded through the ANR-DFG Project NeuroTMR (17-CE19-0021-01) and the CEA-DRF-Impulsion Magnetbrain project. This work was partly supported by the French RENATECH network. The authors thanks Samuel Quest of Femto-ST for his help in the deep RIE etching, Elodie Paul of SPEC-CEA for her support in the magnetrode process, Grégory Cannies of SPEC-CEA for the realization of all the mechanical systems necessary for in-vivo and phantom measurements and Frederike Klein (ESI) for her support during the in vivo experiments. P.F. acknowledges grant support by DFG (SPP 1665 FR2557/1-1, FOR 1847 FR2557/2-1, FR2557/5-1-CORNET, FR2557/6-1-NeuroTMR, FR2557/7-1 DualStreams), EU (HEALTH-F2-2008-200728-BrainSynch, FP7-604102-HBP, FP7-600730-Magnetrodes), a European Young Investigator Award, NIH (1U54MH091657-WU-Minn-Consortium-HCP), and LOEWE (NeFF).

■ ABBREVIATIONS

GMR, giant magneto resistance; SOI, silicon-on-insulator; MR, magneto resistance; rms, root mean square; RTN, random telegraphic noise; LOD, limit of detection

■ REFERENCES

(1) Kandel, E. R.; Schwartz, J. H.; Jessell, T. M. *Principles of Neural Science*, 4th ed.; McGraw-Hill, Health Professions Division, 2000.

(2) Buzsáki, G.; Anastassiou, C. A.; Koch, C. The origin of extracellular fields and currents - EEG, ECoG, LFP and spikes. *Nat. Rev. Neurosci.* **2012**, *13*, 407−420.

(3) Greenebaum, B.; Barnes, F. *Biological and Medical Aspects of Electromagnetic Fields*, 4th ed.; CRC Press, 2018.

(4) Clarke, J.; Braginski, A. I. *The SQUID Handbook: Applications of SQUIDs and SQUID Systems*; John Wiley & Sons, 2004.

(5) Barry, J. F.; Turner, M. J.; Schloss, J. M.; Glenn, D. R.; Song, Y.; Lukin, M. D.; Park, H.; Walsworth, R. L. Optical magnetic detection of single-neuron action potentials using quantum defects in diamond. *Proc. Natl. Acad. Sci. U.S.A.* **2016**, *113*, 14133−14138.

(6) Barbieri, F.; Trauchessec, V.; Caruso, L.; Trejo-Rosillo, J.; Telenczuk, B.; Paul, E.; Bal, T.; Destexhe, A.; Fermon, C.; Pannetier-Lecoeur, M.; Ouanounou, G. Local recording of biological magnetic fields using Giant Magneto Resistance-based micro-probes. *Sci. Rep.* **2016**, *6*, 39330.

(7) Dieny, B.; Speriosu, V. S.; Parkin, S. S. P.; Gurney, B. A.; Wilhoit, D. R.; Mauri, D. Giant magnetoresistive in soft ferromagnetic multilayers. *Phys. Rev. B: Condens. Matter Mater. Phys.* **1991**, *43*, 1297−1300.

(8) Amaral, J.; Gaspar, J.; Pinto, V.; Costa, T.; Sousa, N.; Cardoso, S.; Freitas, P. Measuring brain activity with magnetoresistive sensors integrated in micromachined probe needles. *Appl. Phys. A: Mater. Sci. Process.* **2013**, *111*, 407−412.

(9) Caruso, L.; Wunderle, T.; Lewis, C. M.; Valadeiro, J.; Trauchessec, V.; Trejo Rosillo, J.; Amaral, J. P.; Ni, J.; Jendritza, P.; Fermon, C.; Cardoso, S.; Freitas, P. P.; Fries, P.; Pannetier-Lecoeur, M. In Vivo Magnetic Recording of Neuronal Activity. *Neuron* **2017**, *95*, 1283−1291.

(10) Fermon, C. Introduction on Magnetic Sensing and Spin Electronics. *Nanomagnetism: Applications and Perspectives*; Wiley-VCH: Weinheim, 2017; p 16.

(11) Cardoso, S.; Leitao, D. C.; Dias, T. M.; Valadeiro, J.; Silva, M. D.; Chicharo, A.; Silverio, V.; Gaspar, J.; Freitas, P. P. Challenges and trends in magnetic sensor integration with microfluidics for biomedical applications. *J. Phys. D: Appl. Phys.* **2017**, *50*, 213001.

(12) Murakami, S.; Okada, Y. Contributions of principal neocortical neurons to magnetoencephalography and electroencephalography signals. *J. Physiol.* **2006**, *575*, 925−936.

(13) Silva, A. V.; Leitao, D. C.; Valadeiro, J.; Amaral, J.; Freitas, P. P.; Cardoso, S. Linearization strategies for high sensitivity magnetoresistive sensors. *Eur. Phys. J.: Appl. Phys.* **2015**, *72*, 10601.

(14) Bruno, P. Theory of interlayer magnetic coupling. *Phys. Rev. B: Condens. Matter Mater. Phys.* **1995**, *52*, 411−439.

(15) Nogués, J.; Schuller, I. K. Exchange bias. *J. Magn. Magn. Mater.* **1999**, *192*, 203−232.

(16) Fermon, C.; Pannetier-Lecoeur, M. Noise in GMR and TMR Sensors. *Giant Magnetoresistance (GMR) Sensors*; Springer Berlin Heidelberg: Berlin, Heidelberg, 2013; Vol. *6*, pp 47−70.

(17) Marty, F.; Rousseau, L.; Saadany, B.; Mercier, B.; Français, O.; Mita, Y.; Bourouina, T. Advanced etching of silicon based on deep reactive ion etching for silicon high aspect ratio microstructures and three-dimensional micro- and nanostructures. *Microelectron. J.* **2005**, *36*, 673−677.

(18) Torrejon, J.; Solignac, A.; Chopin, C.; Moulin, J.; Doll, A.; Paul, E.; Fermon, C.; Pannetier-Lecoeur, M. Multiple Giant-Magnetoresistance Sensors Controlled by Additive Dipolar Coupling. *Phys. Rev. Appl.* **2020**, *13*, 034031.

(19) Moulin, J.; Doll, A.; Paul, E.; Pannetier-Lecoeur, M.; Fermon, C.; Sergeeva-Chollet, N.; Solignac, A. Optimizing magnetoresistive sensor signal-to-noise via pinning field tuning. *Appl. Phys. Lett.* **2019**, *115*, 122406.

(20) Quiroga, R. Q.; Nadasdy, Z.; Ben-Shaul, Y. Unsupervised Spike Detection and Sorting with Wavelets and Superparamagnetic Clustering. *Neural Comput.* **2004**, *16*, 1661−1687.

(21) Cao, J.; Freitas, P. P. Wheatstone bridge sensor composed of linear MgO magnetic tunnel junctions. *J. Appl. Phys.* **2010**, *107*, 09E712.

(22) Buzsáki, G. Large-scale recording of neuronal ensembles. *Nat. Neurosci.* **2004**, *7*, 446−451.

(23) Thelin, J.; Jörntell, H.; Psouni, E.; Garwicz, M.; Schouenborg, J.; Danielsen, N.; Linsmeier, C. E. Implant Size and Fixation Mode Strongly Influence Tissue Reactions in the CNS. *PLoS One* **2011**, *6*, No. e16267.